SIMPLIFIED METHODOLOGY TO EVALUATE THE EXTERNAL SULFATE ATTACK IN CONCRETE STRUCTURES

Tai Ikumi[a], Sergio H. P. Cavalaro[a,*], Ignacio Segura[a], Albert de la Fuente[a] and Antonio Aguado[a]

[a] Department of Construction Engineering, Universitat Politècnica de Catalunya Barcelona Tech, Jordi Girona 1-3, C1, E-08034 Barcelona, Spain
* Corresponding author: Sergio H. P. Cavalaro. Department of Construction Engineering, Universitat Politècnica de Catalunya Barcelona Tech, Jordi Girona 1-3, C1, E-08034 Barcelona, Spain. Email address: sergio.pialarissi@upc.edu, Tel: +34 93 401 6507 Fax: +34 93 401 1036

ABSTRACT

The external sulfate attack is a degradation process that causes expansion and cracking in concrete structures. Due to the absence of simplified methodologies to predict the potential damage, codes specify that sulfate resistant cement should be used whenever the surrounding sulfate concentration surpasses a predefined limit. This may lead to penalizing measures as the size of the element or the mechanical properties of the concrete used are not considered. In the present work, an alternative approach is proposed. A simplified chemo-mechanical methodology is deducted to assess the potential damage in concrete elements exposed to sulfate rich environments. Equations to estimate the penetration of sulfates are derived from a numerical model taking into account sulfate consumption, acceleration of the penetration induced by cracking and decrease in diffusivity caused by pore filling. Failure modes associated to this phenomenon are analyzed and a set of equations to assess the risk of failure are deducted. Finally, a parametric study with different geometries of elements and surrounding sulfate contents is performed. The results show that the criterion included in codes might be modified depending on the characteristics of the structure.

Keywords: Concrete; Durability; External sulfate attack; Diffusion; Failure

1.- INTRODUCTION

The external sulfate attack (ESA) is a complex phenomenon in which chemical reactions, ionic transport and mechanical damage interact with each other, leading to expansions and degradation in concrete structures [1-4]. The degradation progresses as sulfate ions from the outside penetrate the element and react with compounds from the hydrated cement paste. As a result, a multi-layered pattern is formed with an external damaged layer and an internal sound core [5]. The mechanical interactions between these zones play a major role in determining the damage induced by the attack.

The ESA has special relevance in underground or foundation structures in contact with sulfate-rich soils. Such structures remain covered during most of their service life, which compromises the early diagnostic of the attack that may only be detected after severe material degradation has occurred. The existing tools to account for potential

46   damage caused by ESA in real structures may be gathered in three main groups:
47   procedures included in building codes, empirical models and integrated models.
48
49   Building codes have traditionally specified precautionary measures to protect concrete
50   against this type of attack. The most common approach is based on the definition of
51   exposure classes regulated by the sulfate content in the media surrounding the structure.
52   Depending on the classification obtained, prescriptions of maximum water/cement ratio,
53   minimum compressive strength and type of cement should be followed to avoid
54   durability problems (e.g. Model Code 2010, BS 8500-1:2006, ACI 201.2R-08, UNE EN
55   206-1:2008). Notice that the size of the element under study or the mechanical
56   properties of the concrete used are not considered. In fact, through the application of
57   this criterion, practitioners are not able to predict the potential damage of the attack or
58   the compliance of a minimum service life. This may lead to penalizing measures and
59   cost overruns as a result of unnecessary use of sulfate resistant cement in some cases.
60
61   Several empirical models have been developed to quantify the spalling depth or the
62   evolution of expansions of concrete elements exposed to ESA. Most of them are based
63   on experience or accelerated laboratory tests performed with small specimens (e.g. [6-
64   8]). The main drawbacks associated with these models are their limited applicability
65   since they are only valid for elements subjected to the same conditions used in the tests.
66   Integrated models take into account the transport of ions, the chemical reaction and the
67   microstructural damage through several differential equations, whose solution
68   commonly require iterative procedures. At present, these models provide the most
69   precise assessment of the ESA. However, the complexity of the equations involved and
70   the high computational cost for their solution may not be accessible to practitioners and
71   certainly are not compatible with the philosophy of most design codes. Besides, the
72   majority of the integrated models from the literature are only capable of predicting the
73   expansion and the damage at a micro-scale level. To estimate the macro-structural
74   response in terms of cracking and failure, advanced structural models should be used,
75   thus compromising even more the straightforward assessment of the attack.
76
77   It is evident that a simplified methodology for the assessment of the potential damage
78   caused by the ESA compatible with the philosophy of building codes is still needed.
79   The objective of this paper is to propose this simplified methodology considering both
80   the micro and macro scale effects. First, the latest integrated models from the literature
81   are analyzed. Based on this, the model by Ikumi et al. [9] is selected and used to derive
82   straightforward equations for the reactive-transport phenomenon accounting for the
83   sulfate consumption, the acceleration of the penetration due to micro-cracking and the
84   decrease in diffusivity due to pore filling. Then, a comprehensive study of the common
85   mechanical failure modes associated with the ESA is presented and a set of simplified
86   equations to assess the failure of the structure are derived. A parametric study is
87   conducted to evaluate the methodology proposed for different geometries under a wide
88   range of realistic field conditions. Based on this study, reference values are proposed for
89   the aluminate content depending on the type and the dimensions of the structure.

90 The methodology developed here represents a step forward on how to assess the ESA
91 explicitly in the design of concrete structures. It allows a more detailed evaluation of the
92 durability of the structures since the specific conditions and expected service life are
93 considered. As a result, an optimized definition of precautionary measures may be
94 obtained for each application.
95
96 **2.- INTEGRATED MODELS**
97
98 Table 1 summarizes some of the integrated models developed during the last decade.
99 This table does not include models that consider ettringite formation through a solid-
100 state mechanism since it is believed that it must occur through solution [10].
101
102 *Table 1. Integrated models developed during the last decade*

Authors	Year	Expansion mechanism	Expansive products
Tixier and Mobasher [11,12]	2003	Volume increase	Ettringite
Bary et al. [13]	2008	Crystallization pressure	Ettringite and gypsum
Sarkar et al. [14]	2010	Volume increase	Ettringite
Idiart et al. [15]	2011	Volume increase	Ettringite
Zuo et al. [16]	2012	Volume increase	Ettringite
Cefis and Comi [17]	2014	Volume increase	Ettringite
Bary et al. [18]	2014	Crystallization pressure/Volume increase	Ettringite
Ikumi et al. [9]	2014	Volume increase	Ettringite
Nie et al. [19]	2015	Volume increase	Ettringite

103
104 Controversy still exists on basic topics of the ESA, especially regarding the expansion
105 mechanism and the gypsum role on the expansion process [3,20]. Amongst the several
106 mechanisms suggested to explain how the precipitation of ettringite leads to expansion,
107 mainly two theories have been implemented in comprehensive models: the volume
108 increase and the crystallization theories.
109
110 According with the first of them, expansions are a result of the additional volume
111 generated by ettringite formation [11,21]. In this case, the response of the matrix and the
112 expansive stresses are calculated from the imposed volumetric strains. According with
113 the second of them, expansions are caused by the crystallization pressure exerted on the
114 pore walls due to the formation of a supersaturated solution within small pores [22,23].
115 In this case, the actual driving pressure that will be translated into strains is obtained by
116 different modifications of the Correns equation [24,25]. Even though the latter theory is
117 supported by recent publications [10,26,27], it requires a very complex chemical
118 approach once the evolution of phases in the pore solution has to be monitored during
119 the attack in terms of chemical activities. Moreover, it was shown by [13] that, despite
120 predicting the cracking state with a relatively good accuracy, this theory leads to
121 macroscopic expansions about two orders of magnitude smaller than the found in
122 experimental data. According to Zhang et al. [28], the reason is that the crystallization
123 pressure assessment is based in an elastic approach that does not account for

124   microcraking and differed deformations (creep), which may play an important role in
125   the final strain measured.

127   In a recent publication [18], Bary et al. tried to solve this issue by introducing an
128   additional macroscopic bulk strain due to the increase of volume produced by secondary
129   ettringite formation. The authors used the equation derived by Tixier and Mobasher [11]
130   and subsequently used by many other researchers [9,14,15]. By adding this
131   consideration, the expansions are a result of both the additional volume generated by
132   ettringite formation and the crystallization pressure exerted on the pore walls by the
133   supersaturated solution. Free expansions calculated with this approach is similar to the
134   obtained in the test of specimens. Bary et al. also pointed out that the contribution of the
135   crystallization pressure is negligibly small compared to the bulk strain produced by
136   secondary ettringite formation [18], which would indicate that the volume increase is
137   the overriding factor in the macroscopic strain evolution.

139   Like Bary et al., other studies from the literature [9] also suggest that the volume
140   increase and the crystallization theories may be compatible as they probably represent
141   two different stages of the sulfate attack. When the solubility limit of ettringite is
142   reached due to the ingress of sulfate ions, the system always tend to return to an
143   equilibrium state through ettringite precipitation. When this energy cannot be released
144   by crystal precipitation, it is released in the form of pressure to the pore walls and the
145   subsequent microcracking as described in the crystallization pressure theory.
146   Microcraking decreases the pressure conditions in the pore, thus allowing ettringite to
147   precipitate near the cracks. Therefore, macroscopic free strains increase proportionally
148   to the amount of ettringite precipitated, being the volume increase inherent to this
149   chemical reaction the driving force of the macroscopic strains. In other words, the
150   initiation of the macroscopic strains arises mainly from the action of the crystallization
151   pressure, while the macroscopic free expansions are explained by the volume increase.

153   Considering that the aim of the present study is to generate simplified models capable of
154   estimating the expansive strain and the failure at a macro-structural level, an integrated
155   model based on the volume increase was selected. This also contributes to a more
156   straightforward approach since a smaller number and simpler input parameters are
157   required to estimate the expansions in the volume increase theory. Therefore, the
158   integrated model by Ikumi et al. [9] was selected as the basis to develop the simplified
159   methodology since it also introduces a more direct and intuitive consideration for the
160   damage assessment and thereby facilitate the definition of the input parameters.

162   It is important to remark that this model only provides the expansion and the damage at
163   a small-scale level. To evaluate the overall response at a macro-scale level and the
164   failure of the structure, Ikumi et al. [9] and other authors suggest that the expansions
165   estimated should be implemented in finite element models that account for the
166   mechanical response of the structure. This represents an important limitation found in

167 practically all integrated models from the literature, which are unable to provide a
168 straightforward verification of the durability of the structure in terms of global failure.
169

170 **3.- SIMPLIFIED METHODOLOGY**

171

172 The methodology proposed in this paper is based on the application of a set of
173 simplified equations to assess the extent of the reactive-transport process and the
174 possible mechanical structural failure at a given service life. As outlined in Figure 1, the
175 aggressiveness of the media and the reactivity of the material define the input
176 parameters for the simplified reactive-transport equations that provide the maximum
177 sulfate penetration and the maximum expansion in the damaged layer of the element.
178 This information combined with the geometric and mechanical characteristics of the
179 element allows the verification of the most common mechanical failure modes. If no
180 mechanical failure occurs and the serviceability is not compromised, it is considered
181 that the structure will comply with the required service life.

182
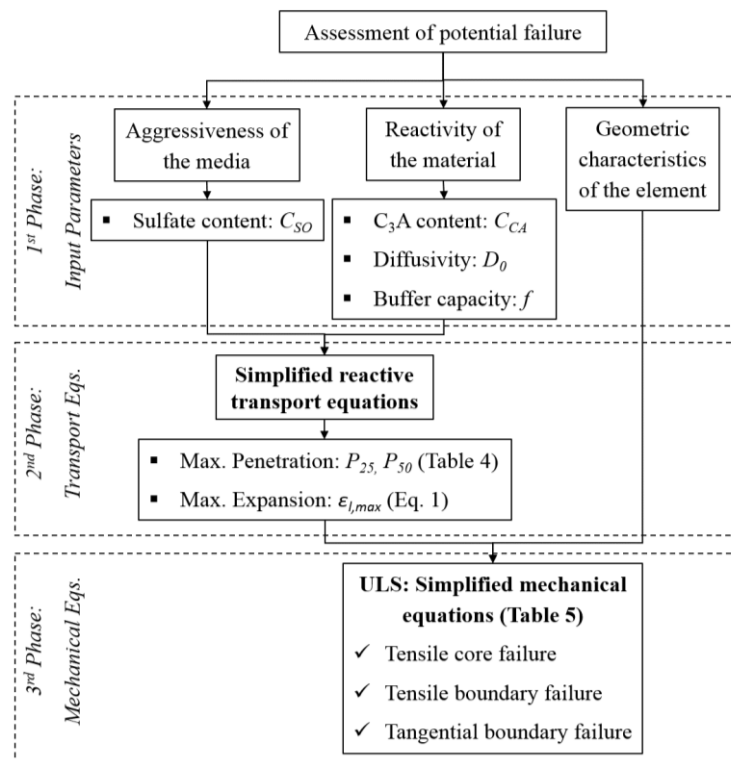
183
184 *Fig. 1. Outline of the simplified methodology for the durability assessment of the ESA*

185

186 3.1- SIMPLIFIED REACTIVE-TRANSPORT EQUATIONS

187

188 In this section, simplified equations to quantify the maximum penetration of the sulfate
189 front and the maximum linear micro-strains at 25 and 50 years are deduced. As these
190 equations are derived from the model described by Ikumi et al. [9], firstly the main
191 features of the model and the hypothesis adopted here are presented.
192 3.1.1 Hypothesis adopted based on the integrated model by Ikumi et al. [9]

193

194 It is assumed that expansions are caused by the volume increase associated to secondary
195 ettringite formation, being the expansive nature of gypsum disregarded. To simplify the
196 model, all hydrated aluminates are considered in the form of monosulfate ($C_4A\bar{S}H_{12}$)
197 since this should be the predominant aluminate phase in hydrated Portland cement
198 pastes at long ages.
199
200 Sulfate and aluminate concentrations are computed through a diffusion-reaction model
201 based on the Fick's second law, which takes into account the ingress of sulfate ions
202 under a concentration gradient and its depletion due to ettringite formation. The
203 effective diffusivity (D) is affected by pore filling, which reduces the paths for
204 additional sulfate diffusion, and micro-cracking and spalling of the cementitious matrix.
205 The latter increases the diffusivity as more paths towards the inner layers may be found.
206
207 The upper bound of the diffusivity reached when the material is completely damaged is
208 set to 10^{-10} m^2/s. This value is slightly below the diffusivity of sulfates in free solution,
209 which Gerard and Marchand [29] quantified as 10^{-9} m^2/s for ions able to move freely
210 within cracks. For the simulations performed in this paper, the value of c_1 and c_2
211 described in [9] were defined respectively as 3 and 6.93, in accordance with the
212 recommendation from [30]. The characteristic cracking length (l_{ch}) is fixed at 26 mm,
213 following the validation by [9].
214
215 Expansions at micro scale are calculated by the additional volume generated by the
216 reaction product ($\Delta V/V$) [21]. This calculation gives a 55% volume increase when
217 monosulfate is converted into ettringite. The total linear strain (ε_l) associated with this
218 expansion is computed by multiplying the expansion factor by the amount of
219 monosulfate reacted ($C_{C_4A\bar{S}H_{12}}^{react}$), as described in Eq. 1. The term M/ρ corresponds to the
220 molar volume of monosulfate and $C_{C_4A\bar{S}H_{12}}^{react}$ is expressed as a molar concentration.
221 Notice that the maximum expansive strain ($\varepsilon_{l.max}$) may be calculated with Eq. 1 by
222 assuming that all monosulfate react to form ettringite.
223

$$\varepsilon_l = \left(1 + \frac{\Delta V}{V}\frac{M}{\rho}C_{C_4A\bar{S}H_{12}}^{react} - f\varphi_0\right)^{1/3} - 1 \qquad (1)$$

224
225 Since ettringite precipitates within the pore network, the matrix is able to accommodate
226 a certain amount of expansive product without exerting any pressure to the pore walls
227 [11,14,31]. Consequently, not all aluminate present will generate expansions. The
228 expression presented by Tixier & Mobasher [11] is used to estimate the buffered
229 expansion. This is represented in the second term of Eq. 1, in which φ_0 is the initial
230 porosity of the matrix and f is the fraction of this porosity that may be filled by
231 expansive products before expansions occur. According with Tixier & Mobasher [11], f
232 usually ranges between 0.05 and 0.40.
233
234

235   3.1.2- Intensification effect in radial fluxes

236

237   In the majority of underground structures subjected to the ESA, the diffusion flux may
238   be classified as approximately linear - typical in diaphragm walls or tunnels - or radial-
239   typical in piled foundations. Transport processes in radial direction are subjected to flux
240   intensification as sulfate penetrates towards the center of the element, concentrating at a
241   smaller area. Conversely, no intensification occurs in a linear flux.

242

243   In a simplified methodology, it is convenient to minimize the number of equations
244   proposed. Therefore, prior to deriving the simplified equations, the sulfate penetration
245   in radial elements is compared with that from linear elements. The aim is to demonstrate
246   that both provide similar results for most real size structures, thus justifying the use of
247   the linear flux formulation for the majority of cases.

248

249   The maximum penetration depths obtained through linear and radial flux approximation
250   were compared for radius ranging from 5 to 50 cm. A minimum sulfate content of 1%
251   of the sulfate concentration in the external surface is defined as a threshold to calculate
252   the penetration depth. Table 2 presents the parameters used in the analysis defined
253   according with the literature. The material used corresponds to a concrete with 350
254   kg/m^3 of cement that contains 80% clinker and 10.8 % of C_3A. Total time simulated is
255   fixed at 25 years. Space intervals of 0.25 mm and variable time steps were considered to
256   ensure stability and convergence.

257

258   *Table 2. Parameters used in the preliminary study of the flux intensification effect*

k [m^3/mol·s]	D_0 [m^2/s]	C_{SO} [mol/m$^3_{water}$] ([g/l])	C_{CA} [mol/m$^3_{concrete}$] ([%C$_3$A])	f_{cm} [MPa]	f	φ_o
0 or 10^{-8}	10^{-12}	34.37 (3.3)	112 (10.8)	30	0.05	0.1

259

260   Figure 2 shows the penetrations depths obtained in the analysis. When no chemical
261   reaction is considered ($k = 0$), the radial and the linear flux provide approximately the
262   same penetration depth for radius of more than 20 cm. The flux intensification observed
263   in radial fluxes reduces the entrance of sulfates and decreases slightly the penetration.
264   This is reasonable since the rate of transfer of a substance in accordance with Fick's
265   second law is proportional to the concentration gradient measured along the diffusion
266   direction. Once the differences in concentrations are smaller in radial fluxes due to the
267   intensification effect, smaller penetration depths should be expected.

268

269   When sulfate depletion caused by the chemical reaction is considered ($k=10^{-8}$
270   m^3/mol·s), the penetration depth is reduced approximately by a factor of 8 in both
271   models. This indicates that chemical reactions are the governing process in the initial
272   stages of the transport phenomenon. In this case, the linear flux and the radial flux
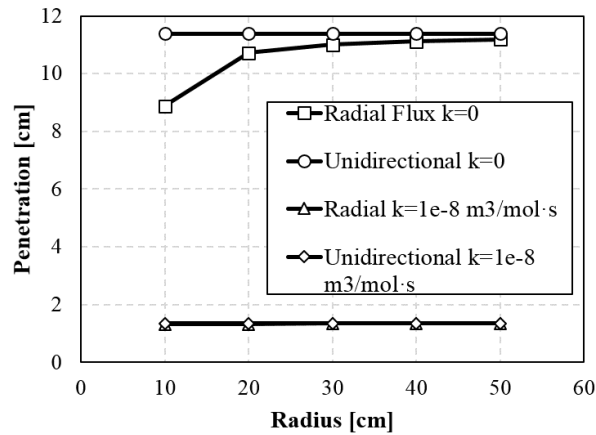273   approaches provide virtually the same results.

Fig. 2. Flux intensification effect

276

277 The analysis performed confirms the small differences between both approaches
278 simulated, especially when the chemical reactions are considered. Moreover, the linear
279 flux approximation provides a prediction of the penetration depth on the safe side given
280 that slightly higher values are obtained. Therefore, in this work a linear flux is adopted
281 for all structural typologies, thus avoiding the definition of two different formulations
282 and the consideration of the element size in the simplified reactive-transport equations.

283

284 3.1.3- Definition of input parameters

285

286 To derive the simplified transport equations, penetration depths obtained through the
287 model by [9] are fitted to a straightforward numerical formulation. Since several
288 parameters are needed in the model by [9], the first step to obtain simplified equations is
289 to detect which of the parameters are the most relevant. For that, a sensibility analysis is
290 conducted with the values defined in Table 3, which are based on recommendations
291 from the literature and found in practice. The range defined for the aluminate content
292 (C_{CA}) correspond to a concrete with 350 kg/m^3 of cement that contain 80% of clinker
293 and from 4% to 12% of C$_3$A. The reference value is equivalent to cement with 8% of
294 C$_3$A.

295

296 *Table 3. Ranges of parameters and penetration front variation in sensibility analysis*

Parameter	Minimum	Reference	Maximum	Penetration depth variation [cm]
C_{SO} [mol/m$^3_{water}$] ([g/l])	6.25 (0.6)	34.37 (3.3)	62.5 (6.0)	1.4
D_0 [m^2/s]	10^{-12}	$5 \cdot 10^{-12}$	10^{-11}	1.4
f [-]	0.0	0.1	0.4	0.8
C_{CA} [mol/m$^3_{concrete}$] ([%C$_3$A])	41 (4)	83 (8)	124 (12)	0.8
φ_o	0.08	0.10	0.14	0.3
f_{cm} [MPa]	20	30	40	0.1

297

298 In practice, the kinetics of the reactions (k) and the temperature might affect the
299 penetration of sulfates. However, nowadays no widely accepted test to quantify this
300 parameter is available. Therefore, it does not seem reasonable to leave the selection of k
301 to the final user. For that reason, k is not considered as a variable in this study. Instead,

a constant k of 10-8 m3/mol·s was selected for all analyses given that other authors traditionally assume values that range from 10-10 to 10-6 m3/mol·s [32].

In the sensibility analysis, a linear flux was simulated considering the same time steps and mesh size of section 3.1.2. Simulations were performed by varying parameters one by one between the maximum and the minimum values, whereas the other parameters were kept equal to the reference values. This procedure is repeated for all parameters from Table 3. In each case, the difference between the penetration depths estimated with the maximum and the minimum values is calculated and presented in Table 3.

The sulfate content and the initial diffusion coefficient are the most influencing parameters. Conversely, the compressive strength and initial porosity show a smaller influence over the penetration depth. Based on these results, C_{SO}, D_0, f and C_{CA} are considered explicitly as input variables of the simplified reactive-transport equations. On the other hand, f_{cm} and φ_o are assumed constant and equal to their reference values for the estimation of the equations that govern the reactive-transport phenomenon (notice that f_{cm} is a variable in the equations developed in later sections to assess the risk of failure).

3.1.4- Proposal of equations

A new study with the model by Ikumi et al. [9] was conducted to derive the simplified reactive-transport equations. At this time, simulations were performed with multiple combinations of the most influencing parameters with several values within the ranges listed in Table 3. More than 2000 simulations were completed at 25 and 50 years. Once a sufficiently big database of penetration depths was obtained, a nonlinear numerical regression was applied to derive the simplified equations that yield the best fit with the numerical results. The final formulations obtained to estimate the penetration depth at 25 and 50 years (P_{25} and P_{50}) are presented in Table 4.

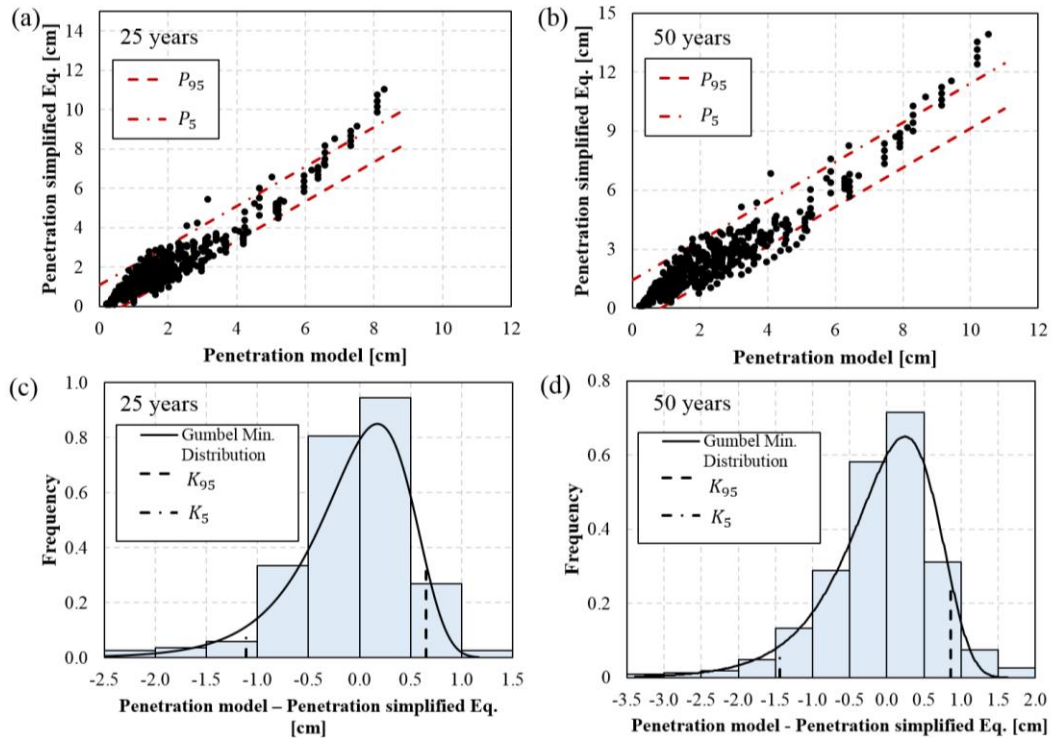*Table 4. Simplified reactive-transport equations*

Service Life [years]	Simplified reactive transport formulation [cm]	K₉₅ [cm]
25	$P_{25} = (7e10D_0 + 0.035C_{SO})\exp\left(\frac{6.65e11D_0+10.737}{C_{CA}} - \frac{1e-10}{35D_o}f\right)$ (2)	0.65
50	$P_{50} = 1.26P_{25}$ (3)	0.86

The initial diffusivity (D_0) is introduced in m²/s, whereas the aluminate content (C_{CA}) is expressed in mol per cubic meter of concrete. The sulfate content (C_{SO}) is expressed in mol of sulfate per cubic meter of water. As these equations are deduced from the model described by Ikumi et al. [9], sulfate consumption, acceleration of the penetration due to cracking and decrease of diffusivity due to pore filling are indirectly considered. Figure 3.a and 3.b depict the correlation between the penetration depths obtained through the integrated model by [9] and with Eq. 2 or Eq. 3. Correlation coefficients of 0.91 and

341 0.90 were obtained, respectively. Notice that both equations are applicable as long as
342 the input parameters remain within the ranges defined in Table 3.
343

344

345 *Fig. 3. Correlation between penetration obtained with integrated model and simplified*
346 *equation (a and b); Gumbel distribution to assess error of estimation (c and d)*

347

348 Even though the simplified reactive-transport equations provide a fair approximation of
349 the integrated model, in some situations it might be necessary to use estimations on the
350 safe side. Therefore, a statistical analysis was performed in order to assess the error of
351 prediction of Eq. 2 and Eq. 3. As shown in Figures 3.c and 3.d, the frequency of the
352 error of estimation was fit to a Gumbel distribution (minimum extreme value type I).
353 Then, the distribution was used to assess the minimum penetration depth that had to be
354 summed to the obtained with the simplified equations in order to assure a 95% of
355 probability of achieving values above the calculated with the integrated model by [9].
356 This additional value (K_{95}) is shown in Table 4 and should be directly added to Eq. 2
357 and Eq. 3 in case a safer estimation is required.

358

359 For the chemical reaction rate (k) considered in the literature, it has been demonstrated
360 that the aluminates of the exterior layers are rapidly consumed by the ingressing sulfates
361 [9]. This means that the maximum expansive strain ($\varepsilon_{l.max}$) is rapidly reached at the
362 surface layers of the element. Once the aluminates are consumed, the sulfates advance
363 at a higher rate to the inner layers, reacting with new aluminates present. Hence, an
364 abrupt variation of the expansion should occur close to the penetration front.

365

366 Figure 4 shows in continuous lines the typical strain profiles due to ESA in structures
367 under symmetric (sulfate insource from all sides) or asymmetric sulfate exposure

conditions (sulfate insource from only one side). To simplify the structural consideration of the ESA, the strain profile depicted with the red discontinuous line is used instead. It assumes that $\varepsilon_{l.max}$ estimated with Eq. 1 occurs along the whole penetration depth obtained with Eq. 2 or Eq. 3, which is a hypothesis on the safe side.
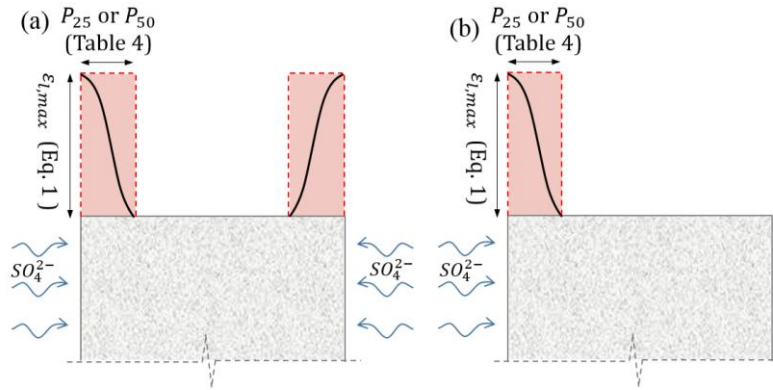
Fig. 4. Strain profiles for symmetric (a) and asymmetric (b) sulfate exposure

3.2- SIMPLIFIED MECHANICAL EQUATIONS

Although expansion due to ettringite formation is concentrated in the surficial layers, strains also appear in the sound core of the element to maintain compatibility. In fact, the sound core acts as a restriction that reduces the expansion calculated with Eq. 1. An auto-balanced tension state is generated, leading to possible mechanical failures outside the zone directly affected by the sulfate penetration and by the attack. Three failures modes are distinguished: tensile failure of the sound core, tangential failure and tensile failure in the boundary between the surficial layers and the sound core.

Micro-cracks in the external layers of the element due to high compressive stresses are usually developed prior to any failure mode. Generally, the micro-cracking is localized, affecting only a few millimeters closer to the surface. Therefore, it is not considered a failure mode as it does not imply the macro-structural failure of the element. The superficial micro-cracking modifies the local mechanical properties and the sulfate diffusion coefficient. This phenomenon is taken into account in the simplified methodology by a degradation of the elastic modulus and an increase in the diffusion coefficient in the zone directly affected by the sulfate penetration. Notice that interactions with other elements in contact with the structure directly under attack (such as external loads or strain constraints in specific directions) could modify the stresses profile and affect the failure. However, these considerations cannot be included in a simplified methodology as they will vary depending on each study case.

3.2.1- Tensile failure of the sound core

The expansions of the outer layers along the length of the element are restrained due to the stiffness provided by the sound inner core. This causes normal compressive stresses

403 (σ_c) at the surficial layers, while normal tensile stresses (σ_{tc}) appear at the sound inner
404 core. If σ_{tc} reaches the tensile strength of concrete, the inner core might crack, reducing
405 significantly the restrains applied to the external layers. This might produce a release of
406 the restricted strains and an abrupt displacement of the structure. In Figure 5, such
407 situation is represented before and after cracking for elements under symmetric and
408 asymmetric sulfate exposure conditions.
409
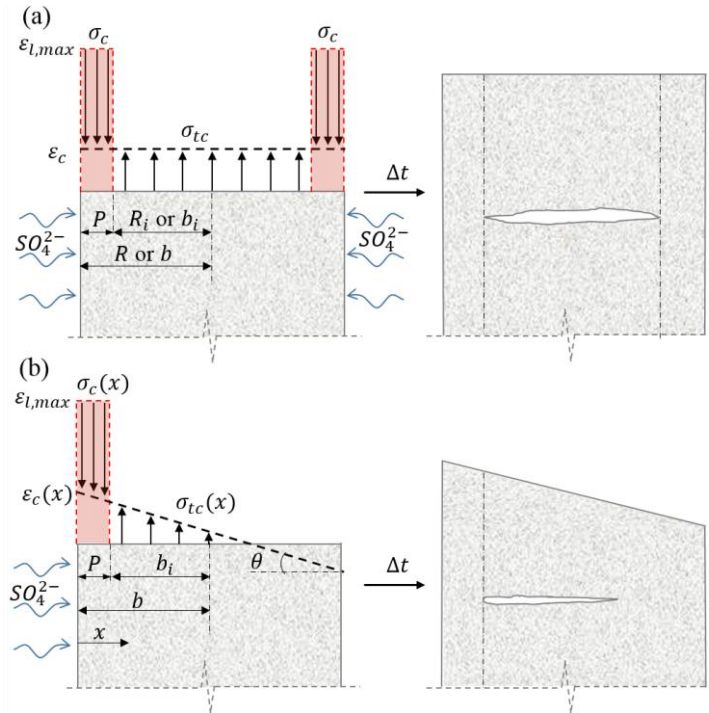
411 *Fig. 5. Normal stress distribution in symmetric (a) and 1 face (b) sulfate exposure.*

413 As an approximation, it is assumed that the Navier-Bernouilli hypothesis applies to the
414 cross-section of the element. This means that the original cross-section (before any
415 expansion occurs) should remain plane after the expansions take place. Consequently,
416 the final strain (ε_c) of the cross-section should follow the profile depicted as a
417 discontinuous line in Figure 5. By imposing equilibrium in a simple sectional analysis
418 (Eq. 4 to 6), it is possible to assess σ_c and σ_{tc}.
419

$$N = 0 = \int_{Area} E(x) \cdot \big(\varepsilon_c(x) - \varepsilon_l(x)\big) \partial Area \qquad (4)$$

$$M = 0 = \int_{Area} E(x) \cdot \big(\varepsilon_c(x) - \varepsilon_l(x)\big) x \partial Area \qquad (5)$$

$$\varepsilon_c(x) = \varepsilon_c(x = 0) + \zeta x \qquad (6)$$

421 The term ζ (<<1) represents the curvature of the cross-section. The stress level is
422 calculated with Eq. 7 by multiplying the elastic modulus of the material (E) and the
423 difference between the total strain (ε_c) and the non-mechanical strain (ε_l).
424

$$\sigma(x) = E(x) \cdot [\varepsilon_c(x) - \varepsilon_l(x)] \qquad (7)$$

425

426 The value of E is affected by the damage induced by the ESA, varying along the cross-
427 section. In this sense, the sound core presents an elastic modulus E_0 that should be
428 higher than the elastic modulus E_e of the external layer affected by microcracking. To
429 account for this effect on the structural formulation, E_e is assumed constant along the
430 external layer, whereas E_0 is set constant in the sound core. Even though no consensus
431 exists in the literature on the quantification of the degradation of mechanical properties,
432 most studies suggest that the strength loss for specimens may range between 10-50%
433 [33,34].

434

435 Creep deformations were not considered in the simplified methodology proposed here
436 as this implies an iterative calculation that would compromise the straightforwardness
437 of the approach. Notice that creep deformations would reduce the internal stress level of
438 the structural element, allowing the accommodation of part of the expansions.
439 Therefore, disregarding creep effects is a simplification on the safe side since it would
440 lead to the calculation of higher stresses than the expected in reality. However, this
441 assumption also affects the assessment of the displacements and the verification of the
442 serviceability limit state since smaller strain levels than the expected in reality would be
443 obtained with the formulation proposed here. If high precision is required in the
444 assessment of the displacement, differed strains should be taken into account.

445

446 By solving Eq. 4 to 6 for different structural typologies and sulfate exposures, Eq. 8 to
447 10 are obtained to predict the maximum tensile stresses acting at a certain time in the
448 cross-section (see Table 5). In the case of piles, R represents the total radius of the
449 cross-section and R_i is the radius of the sound core given by the difference between R
450 and the penetration depth P calculated with Eq. 2 or 3. In the case of diaphragm walls or
451 tunnels, b represent the half thickness of the element.

452

453 *Table 5. Simplified equations to predict the maximum stresses due to ESA*

Struct. typology	Sulfate exposure	Tensile failure of the sound core	Tangential boundary failure	Tensile boundary failure
Piles (linear elements)	Full	$\sigma_{tc} = \frac{E_0 E_e \varepsilon_l (R^2 - R_i^2)}{E_e (R^2 - R_i^2) + E_0 R_i^2}$ (8)	$\tau_b = \frac{E_0 E_e \varepsilon_l (R^2 - R_i^2) R_i \beta_r}{2(E_e(R^2 - R_i^2) + E_0 R_i^2)} tanh\left(\frac{\beta_r l}{2}\right)$ (13)	$\sigma_{tb} = \frac{\varepsilon_l E_e P}{R_i}$ (17)
Diaphragm walls or tunnels (surface elements)	2 faces	$\sigma_{tc} = \frac{E_0 E_e \varepsilon_l P}{E_e P + E_0 (b-P)}$ (9)	$\tau_b = \frac{E_0 E_e \varepsilon_l P b_i \beta}{E_e P + E_0 (b-P)} tanh\left(\frac{\beta l}{2}\right)$ (14)	-
	1 face	$\sigma_{tc} = \frac{E_0 \varepsilon_l P (3P^2 - 9Pb + 8b^2)}{4b^3}$ (10)		

454

455 All equations included in Table 5 are able to assess mechanical failures at any time, as
456 long as the penetration of sulfates are provided. The different mechanical failure modes
457 considered and the corresponding stresses are treated separately in this paper. Even
458 though a certain interaction might occur, it was assumed that one of the failure modes

459 would happen because of the predominant stress. In case a more accurate prediction of
460 the structural failure is needed, stresses from different mechanisms should be treated in
461 a coupled way and more advanced simulations should be performed, for instance with
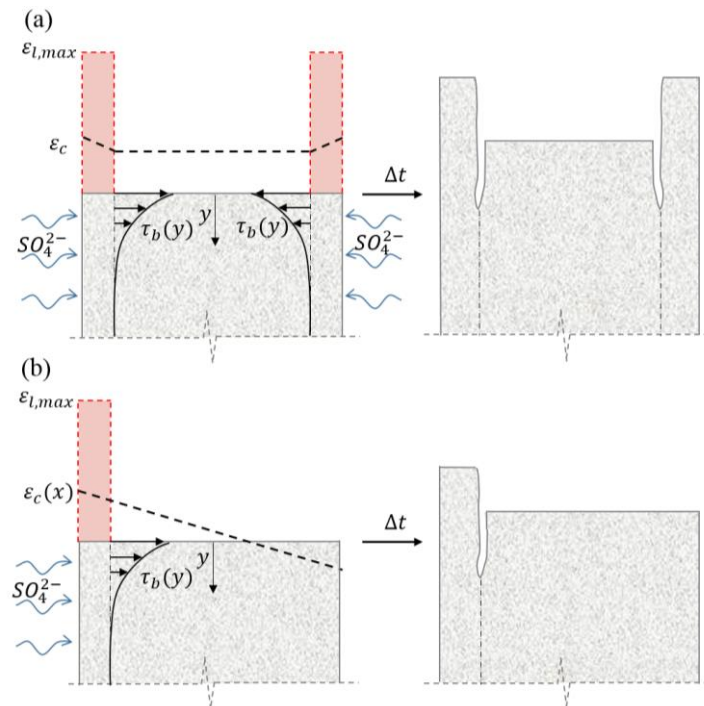462 coupled FEM.
463
464 3.2.2- Tangential boundary failure
465
466 Experimental studies show that mortar prisms exposed to ESA tend to present a layered
467 spalling of the surface [5,15]. One of the possible mechanisms responsible for this
468 phenomenon is depicted in Figure 6.
469

471 *Fig. 6. Tangential stress distribution in symmetric (a) and 1 face (b) sulfate exposure.*

472

473 Even though at intermediate sections the normal stresses distribution described in
474 section 3.2.1 guarantees the compatibility of the deformation, at the top free cross-
475 section of the element the compatibility has to be achieved through alternative
476 mechanisms since no normal stresses exist. The difference in terms of vertical
477 displacement creates tangential stresses between the surface layers affected by the ESA
478 and the sound core. These should guarantee the compatibility of displacements at the
479 extremities of the element. If the tangential stresses reach the tangential strength of the
480 material, cracks might appear leading to the failure of the structure.

481

482 In this study, an analogy with the classical Mixing Theory for short fibers is applied
483 [35-37] in order to deduct the equations to assess the tangential stresses. By imposing
484 equilibrium and compatibility, Eq. 11 is obtained to estimate the tangential stresses (τ_b)
485 between the sound core and the surface layers at the position y along the axis of a pile.
486 In this equation, l is the length of the element, β_r is a coefficient given by Eq. 12 and G

487   is the elastic shear modulus of concrete, which may be estimated from the elastic
488   modulus. The maximum tangential stresses are located at the extremities of the element
489   so that y should be substituted by 0 in Eq. 11. This gives Eq. 13 (see Table 5) for the
490   assessment of the maximum tangential stresses in piles.
491

$$\tau_b(y) = \frac{E_0 \varepsilon_c R_i \beta_r}{2} \frac{sinh\left[\beta\left(\frac{l}{2} - y\right)\right]}{cosh\left(\beta\frac{l}{2}\right)} \tag{11}$$

$$\beta_r = \sqrt{\frac{2G}{E_0 R_i^2 ln\left(\frac{R}{R_i}\right)}} \tag{12}$$

492
493   Analogous deductions may be performed for diaphragm walls or tunnels. Eq. 14 is
494   obtained for such elements exposed to sulfates at 2 faces (see Table 5). The parameter β
495   should be calculated according with Eq. 15. The same formulation is also adopted when
496   elements are exposed to the sulfate ingress only in one face. The curvature introduced
497   by the asymmetric load increases the macroscopic strain in the external damaged layer
498   and reduces the compressive stresses in this region. Therefore, the tangential stresses
499   transmitted to the sound core are reduced, leading to an assessment on the safe side.
500

$$\beta = \sqrt{\frac{G}{E_0(b - P)P}} \tag{15}$$

501
502   It is important to remark l only affects the assessment of the tangential stresses if the
503   length of the element is below a critical value (around 1 m for most structures). For
504   bigger values of l, the maximum tangential stress at the extremities of the element will
505   remain approximately constant. Therefore, the parameter l would not affect the stresses
506   calculated in most structures.
507
508   3.2.3- Tensile boundary failure
509
510   In linear structures exposed all around to sulfates, the layered spalling may also be
511   caused by a tensile boundary failure. As shown in Figure 7, tensile stresses (σ_{tb}) are
512   induced by the restrictions of the sound core to the expansions experienced by the
513   affected layer in the cross-sectional plane. Cracks appear if the stresses reach the tensile
514   strength of concrete.
515
516   Since the penetration depth tend to be significantly smaller than the radius of the
517   element, an analogy with the thin-walled cylinders subjected to internal pressure may be
518   made. The affected external layer would tend to present an expansion $\varepsilon_{l,max}$ due to the
519   ESA. This would generate stresses in the interface with the inner core, which would
520   deform by ε_{ce} along the diameter of the element. The restriction generates compressive
521   stresses at the external surface affected by the ESA equal to $E_e(\varepsilon_{l,max} - \varepsilon_{ce})$.
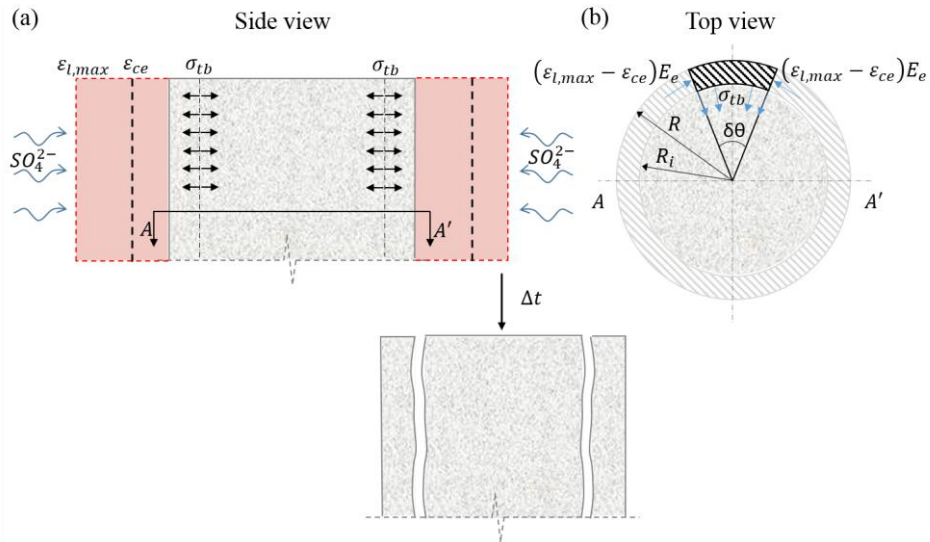
523   *Fig. 7. Side view (a) and top view (b) of tensile stresses due to restrain of expansions in the cross-*
524   *sectional plane*

525

526   These compressive stresses should be balanced by the tensile stresses σ_{tb} acting in the
527   interface with the sound core, as shown in Figure 7.b. By imposing equilibrium of the
528   in-plane forces, Eq. 16 is obtained. Maximum tensile stresses occur when the external
529   surface of the element is totally restrained by the sound core, that is, ε_{ce} equals 0. This
530   gives Eq. 17, which should be used for the assessment of σ_{tb} (see Table 5).

$$\sigma_{tb} = \frac{PE_e(\varepsilon_{l.max} - \varepsilon_{ce})}{R_i} \qquad (16)$$

531

532   **4.- PARAMETRIC STUDY**

533

534   A parametric study is performed to evaluate the results provided by the simplified
535   methodology under a wide range of realistic conditions found in practice. Different
536   sulfate concentrations in the media, aluminate contents and size of elements were
537   evaluated. The results obtained are compared to those calculated with the integrated
538   model by [9] and to the criteria from structural codes.

539

540   Table 6 shows the ranges and the reference values assumed for the two parameters
541   considered in the study. All sulfate concentrations (C_{SO}) evaluated correspond to
542   moderately or highly aggressive exposure classes according to UNE EN 206-1. The
543   range defined for the aluminate content (C_{CA}) correspond to a concrete with 350 kg/m^3
544   of cement that contain 80% of clinker and from 4% to 12% of C$_3$A. The reference value
545   is equivalent to cement with 10% of C$_3$A. Initial diffusivity and the buffer capacity of
546   the matrix are initially fixed at 10^{-12} m^2/s and 0.15, respectively. The length (l) of the
547   structural element is fixed at 5 m, which is above the critical length for the assessment
548   of the tangential stresses. This means that the results derived from the parametric study
549   also apply to elements with bigger values of l. The additional input parameters required
550   in the integrated model by [9] are fixed at the reference values adopted in section 3.1.3.

551

Table 6. Range of parameters in the parametric study

Parameter	Minimum	Reference	Maximum
C_{SO} [g/l]	0.6	3.0	4.2
C_{CA} [% C_3A]	4	10	12

The compressive strength and the elastic modulus of concrete are fixed at 30 MPa and 28000 MPa, respectively. The elastic modulus was considered the same at the sound core and at the superficial layer affected by ESA. This consideration is on the safe side since it provides higher internal stresses in the equations from Table 5. The tensile strength (f_t) of the material is approximated through the formulation included in the Model Code. The formulation proposed by Kaneko et al. [38] is used to estimate the shear strength, which gives a τ_{max} of 7.1 MPa. This value is in agreement with experimental tests performed by Djazmati [39].

4.1.- INFLUENCE OF C_{SO}

Figure 8 shows the penetration depth at 25 and 50 years obtained with the integrated model by Ikumi et al. [9] and with the simplified equations (Eq. 2 and 3) for different sulfate concentrations. The curves corresponding to the simplified equations with the 95% probability (K_{95}) are depicted in dotted lines. At both ages, the simplified equations derived in this study provide a good fit of the penetration front. The use of K_{95} yields penetration depths above the expected values, ensuring conservative results.
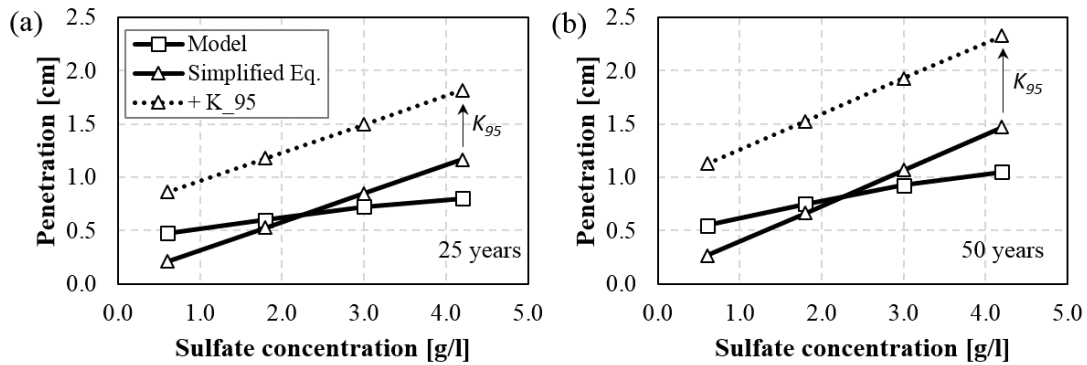
*Fig. 8. Penetration depth for different sulfate concentrations*

To evaluate the risk of mechanical failure, the maximum linear expansions ($\varepsilon_{l.max}$) are calculated with Eq. 1, assuming that all aluminate react to form ettringite. This gives a $\varepsilon_{l.max}$ of $8.7 \cdot 10^{-4}$. Simplified equations presented in Table 5 for piles under full sulfate exposure are applied to calculate the tensile stress in the sound core (σ_{tc}), the tangential stress (τ_b) and the tensile stress (σ_{tb}) between the damaged and undamaged areas. Only penetration depths obtained through the simplified equation are evaluated. The ratio between each stress and the corresponding strength is calculated through Eq. 18 to 20 to make the risk of failure comparable for the different modes analyzed. The failure occurs if any of the ratios become bigger than 1.

$$\psi_{Tensile\ core} = {\sigma_{tc}}/{f_t} \qquad (18)$$

$$\psi_{Tangential} = {\tau_b}/{\tau_{max}} \qquad (19)$$

$$\psi_{Tensile\ boundary} = {\sigma_{tb}}/{f_t} \qquad (20)$$

584   Figure 9 shows the stress/strength ratios at 25 and 50 years for piles with 90 cm, 40cm
585   and 30 cm of diameter under different sulfate exposure conditions. In these figures, the
586   limit of failure is depicted with a discontinuous line.
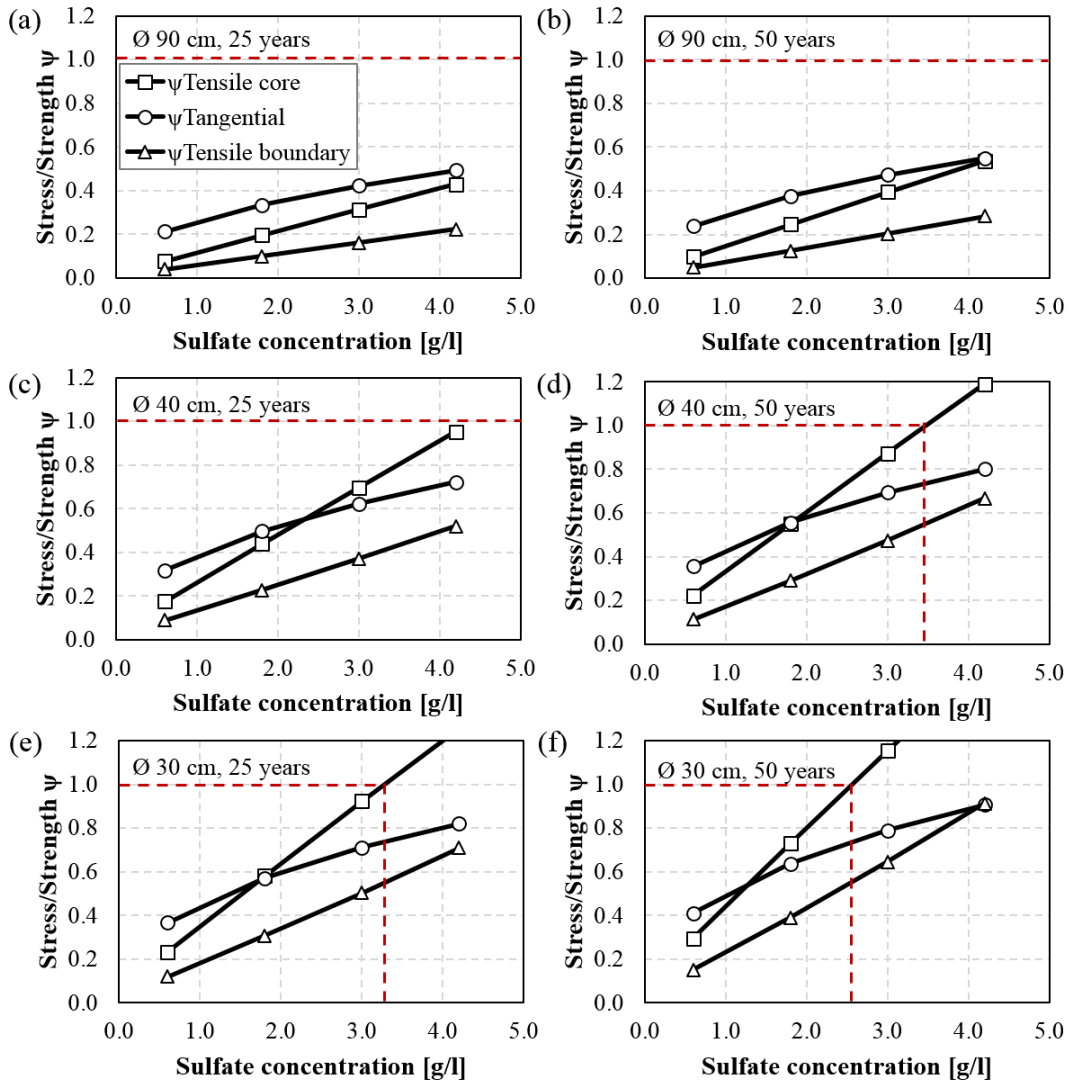
587

588   *Fig. 9. Stress/strength ratio for different sulfate concentrations*

589

590   Results for piles with 90 cm of diameter (Figures 9.a and 9.b) indicate no mechanical
591   failure for any sulfate concentration below 4.2 g/l. The highest ratios are found for
592    $\psi_{Tangential}$, followed by $\psi_{Tensile\ core}$ and $\psi_{Tensile\ boundary}$. In piles with 40 cm of
593   diameter, $\psi_{Tangential}$ are the highest for low sulfate exposure conditions, while
594    $\psi_{Tensile\ core}$ become critical in severe sulfate exposure conditions. In fact, a tensile
595   failure of the sound core may occur for sulfate concentrations above 3.4 g/l at 50 years
596   (Figure 9.d). Likewise, for piles with 30 cm of diameter, failure occurs according with

597　the same mechanism for sulfate concentrations above 2.6 g/l and 3.3 g/l at 25 and 50
598　years, respectively (Figures 9.e and 9.f).
599
600　Results suggest that, for low sulfate concentrations, failure is likely to occur due to
601　tangential stresses that causes surface delamination. Conversely, for higher sulfate
602　concentrations, failure is likely to occur due to the tensile stresses at the sound core that
603　causes cracking at the cross-section. This distinction is relevant since delamination of
604　exterior layers may be accepted as long as it does not compromise the safety of the
605　structure or the protection of the steel rebar. On the contrary, cracking of the cross-
606　section should be taken with care especially in piles subjected to moments or to tensile
607　forces.
608
609　Notice that according to the European standard UNE EN 206-1, the 10% C_3A cement
610　used in this parametric study is not allowed for sulfate concentrations above 0.6 g/l,
611　regardless of the size of the pile. The estimations performed indicate that the limit
612　established in the codes may be modified depending on the size of the element, the
613　cement content and the mechanical properties of the concrete used in each application.
614
615　4.2.- INFLUENCE OF C_3A CONTENT
616
617　Penetration depths predicted with the integrated model by Ikumi et al. [9] and with the
618　simplified equations derived in this work are compared in Figure 10 for different C_3A
619　contents at 25 and 50 years. Again, the simplified equations provide a good fit of the
620　penetration depths at both ages. As described in section 4, the aluminate content has
621　minor influence on the penetration front. However, it is one of the main parameters that
622　define the magnitude of the maximum expansion in Eq. 1.
623
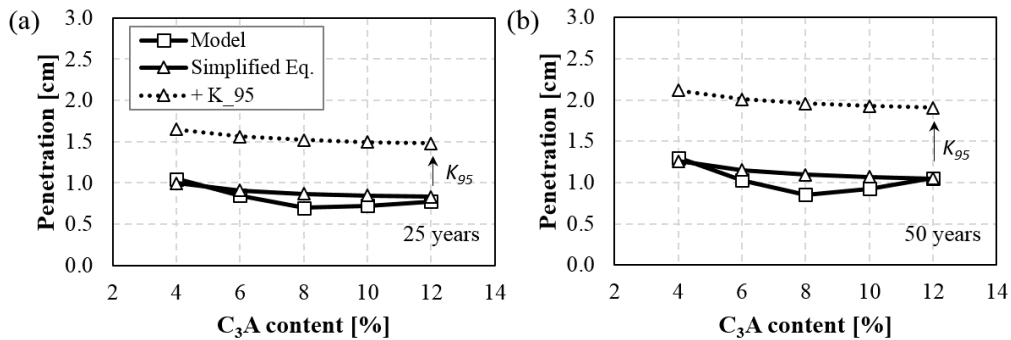
625　*Fig. 10. Penetration depth for different aluminate contents*

626
627　Figure 11 presents the stress/strength ratios for several C_3A contents in piles with 90
628　cm, 40cm and 30 cm of diameter at 25 and 50 years. All curves present a similar trend,
629　showing no failure for low contents of C_3A. Once a threshold content is reached, all
630　stress/strength ratios increase abruptly, indicating a high risk of failure. This trend is in
631　agreement with the criteria included in structural codes, which establish a limiting C_3A
632　content for sulfate resistant cements (usually 5% to 6%). Below this limit it is assumed
633　that no unacceptable damage will take place. The fact that this criterion has been

634 successfully applied in many structural elements worldwide suggests that the simplified
635 formulation proposed here is capable of reproducing the general behavior of concrete
636 structures subjected to sulfate attack.
637
638 Results in piles with 90 cm of diameter indicate failure due to tangential stresses for
639 C_3A contents above 12%. In piles with 40 cm and 30 cm of diameter, a tensile core
640 failure is predicted for C_3A contents around 10%. It is evident that the C_3A threshold
641 depends on the size of the element, the cement content and the mechanical properties of
642 the concrete.
643
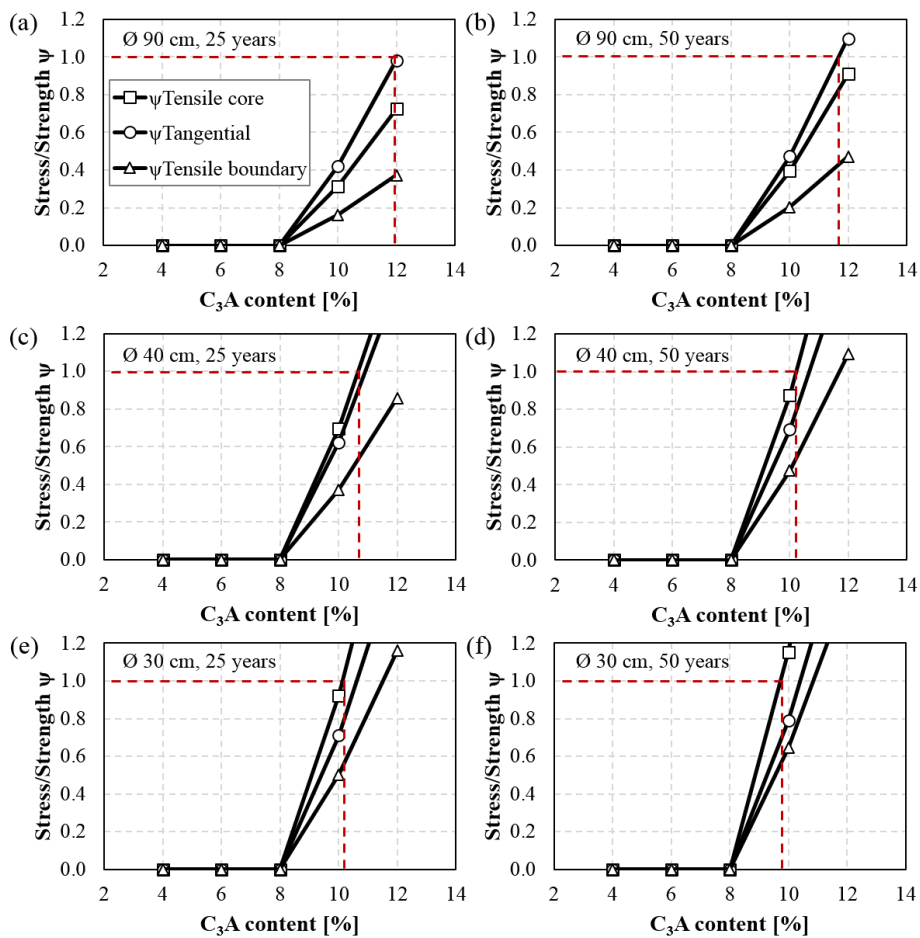
645 *Fig. 11. Stress/strength ratio for different C_3A contents*
646
647 4.3.- INFLUENCE OF BUFFER CAPCITY (*f*)
648
649 Figure 12 shows the thresholds obtained for different pile diameters, buffer coefficients
650 and sulfate exposure conditions at 25 and 50 years. Values above 12% and below 4%
651 are not depicted since are beyond the range used to deduct the simplified formulation.
652
653 The results show that the increase in the diameter of the pile leads to an increase of the
654 C_3A threshold. Nevertheless, the main parameter governing the C_3A threshold is the
655 buffer coefficient (*f*). According with Tixier and Mobasher [11], *f* may vary between
656 0.05 and 0.40. However, the results obtained suggest that values above 0.20 are not

657 realistic, as the matrix is able to accommodate enough expansive products without any
658 macro-structural damage for all exposure conditions considered. Therefore, a buffer
659 capacity around 0.10 is proposed in the present study.
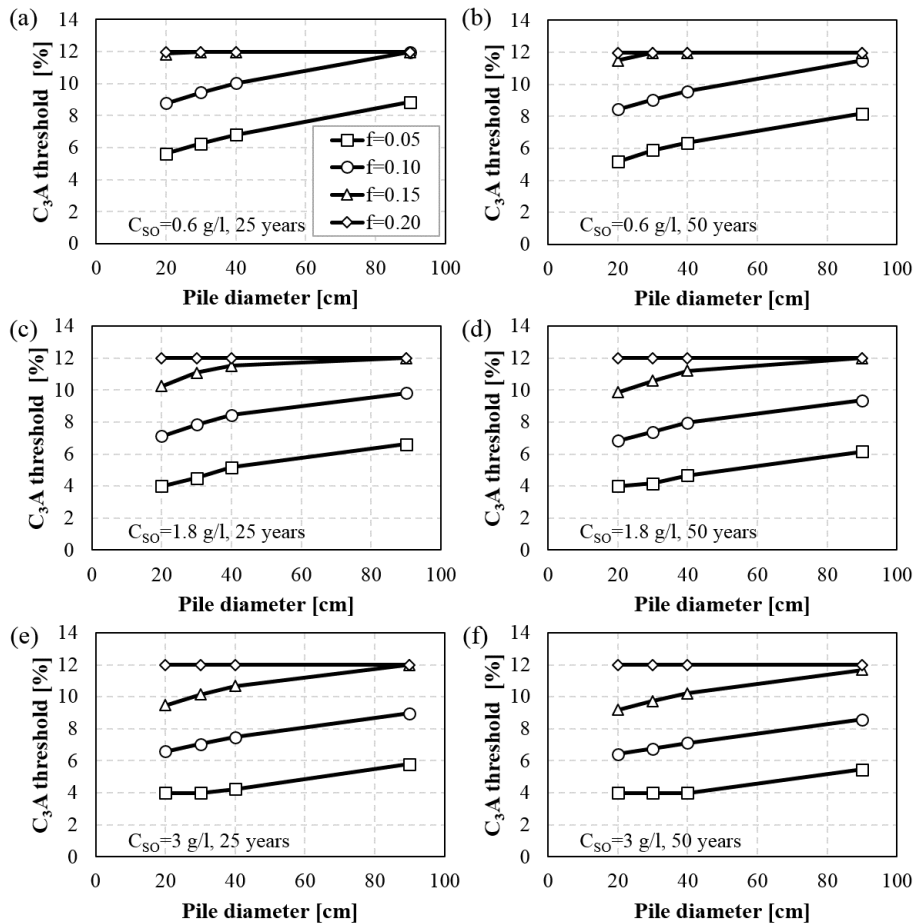
660

661 *Fig. 12. C$_3$A threshold for different pile diameters and buffer coefficients*

662

663 4.4.- PROPOSED C$_3$A THRESHOLD FOR PILES

664

665 Reference C$_3$A threshold values calculated with the simplified model are presented for
666 different exposure conditions and dimensions for service lives of 25 and 50 years. Table
667 7 corresponds to radial elements –piles-, whereas Table 8 and Table 9 correspond to
668 elements such as walls under full or partial exposure, respectively.

669

670 *Table 7. Proposed % C$_3$A threshold for a service life of 25 years and 50 years (in*
671 *brackets).*

C_{so} [g/l]	Pile diameter [cm]			
	20	**30**	**40**	**90**
0.6	8.8 (8.4)	9.4 (9.0)	10.0 (9.6)	≥12.00 (11.5)
1.8	7.1 (6.8)	7.8 (7.4)	8.4 (8.0)	9.8 (9.4)
3.0	6.6 (6.4)	7.0 (6.8)	7.5 (7.1)	8.9 (8.6)
4.2	6.3 (6.2)	6.7 (6.5)	7.0 (6.7)	8.5 (8.0)

672

Table 8. Proposed % C₃A threshold for a service life of 25 years and 50 years (in brackets) in surface elements with.2 faces exposed.

C_{So} [g/l]	Surface element width [cm]			
	20	**30**	**40**	**90**
0.6	10.0 (9.6)	11.0 (10.4)	11.9 (11.2)	≥12.0 (≥12.0)
1.8	8.5 (7.9)	9.1 (8.7)	9.6 (9.2)	11.5 (10.9)
3.0	7.4 (7.1)	8.3 (7.8)	8.8 (8.5)	10.3 (9.8)
4.2	7.0 (6.7)	7.6 (7.2)	8.2 (7.7)	9.6 (9.2)

Table 9. Proposed % C₃A threshold for a service life of 25 years and 50 years (in brackets) in surface elements with.1 face exposed.

C_{So} [g/l]	Surface element width [cm]			
	20	**30**	**40**	**90**
0.6	9.4 (8.6)	11.0 (10.1)	11.9 (11.2)	≥12.0 (≥12.0)
1.8	7.2 (6.9)	7.9 (7.5)	8.6 (8.0)	11.5 (10.9)
3.0	6.7 (6.5)	7.1 (6.8)	7.5 (7.2)	9.8 (9.0)
4.2	6.4 (6.3)	6.7 (6.5)	7.1 (6.8)	8.7 (8.1)

The values recommended in Tables 7 to 9 are applicable to concretes with 350 kg of cement per cubic meter, an *f* equal to 0.10, the sulfate diffusivity and concrete mechanical properties considered in the parametric study. Once more the values confirm that the C₃A threshold depends on the dimensions of the element and the exposure conditions. It is also observed that for equivalent conditions the threshold for piles tends be smaller than that obtained for walls or tunnels. This is the result of the bigger ratio between exposed surface and the total volume found in piles.

In case a different cement content is used, the values from all tables should be multiplied by 350 and divided by the actual content in kg per cubic meter of concrete. Moreover, in case an *f* equal to 0.05 should be considered, the values from Tables 7, 8 and 9 should be multiplied by 0.63, 0.66 and 0.60, respectively.

5.- CONCLUSIONS

A simplified methodology that considers the transport-reaction and the damage at a macro-structural level due to the ESA was proposed. This methodology allows a direct and simple assessment of the risk of failure for elements (piles, walls and tunnels) exposed to a sulfate rich environment, considering the conditions found in each application. The following conclusions may be derived from this study.

- Flux intensification effect of the sulfate ions in radial elements plays a minor role in the maximum penetration depth for the typical size of real structures. Therefore, unidirectional flux is adopted for all structural typologies, thus avoiding the use of different formulations and the consideration of the element size in the simplified reactive-transport equations.

- Sulfate and aluminate concentration, initial diffusivity and the buffer coefficient are the most influencing parameters for the estimation of the penetration front. Changes in the compressive strength and initial porosity display a smaller influence on the penetration depth.
- According to the results obtained, buffer capacities above 0.20 of the initial porosity are not realistic. Therefore, buffer capacities between 0.05 and 0.20 should be used.
- For lower sulfate concentrations and bigger pile diameters, failure is likely to occur due to tangential stresses that causes surface delamination. On the other hand, for bigger sulfate concentrations and lower pile diameters, failure is likely to occur due to the tensile stresses at the sound core that causes cracking at the cross-section.
- The simplified methodology suggests the existence of a C_3A threshold above which a high risk of structural damage occurs. This trend is consistent with the philosophy used in structural codes and validated in practice. The C_3A threshold increases with the increase of the size of the element and with the reduction of the sulfate concentration.
- Reference values are proposed for the C_3A threshold depending on the exposure conditions, type and dimensions of the structure. In case a more precise assessment is required, the equation included in the simplified methodology may be used to estimate the C_3A threshold. The procedure followed for this estimation requires the use of the formulation included in Tables 4 and 5, being compatible with the durability assessment found in building codes.

ACKNOWLEDGMENTS

REFERENCES.

[1]   C. Ayora, S. Chinchón, A. Aguado, F. Guirado, Weathering of iron sulfides and concrete alteration: Thermodynamic model and observation in dams from central Pyrenees, Spain, Cem. Concr. Res. 28 (1998) 591–603.

[2]   J.P. Skalny, I. Odler, J. Marchand, Sulfate Attack on Concrete, Spon, London, (2001).

[3]   A. Neville, The confused world of sulfate attack on concrete, Cem. Concr. Res. 34 (2004) 1275–1296.

[4]   J.S. Chinchón, C. Ayora, A. Aguado, F. Guirado, Influence of weathering of iron sulfides contained in aggregates on concrete durability. Cem. Concr. Res. 25 (1995) 1264-1272.

747   [5]   S.T. Lee, R.D. Hooton, H. Jung, D. Park, C.S. Choi, Effect of limestone filler on

748   the deterioration of mortars and pastes exposed to sulfate solutions at ambient

749   temperature, Cem. Concr. Res. 38 (2008) 68–76.

750   [6]   A. Atkinson, J.A. Hearne, An assessment of the long-term durability of concrete

751   in radioactive waste repositories, MRS Proceedings 50 (1985) 239.

752   [7]   A. Atkinson, J.A. Hearne, Mechanistic model for the durability of concrete

753   barriers exposed to sulphate-bearing groundwaters, Mat. Res. Soc. Symp. Proc. 176

754   (1990) 149-156.

755   [8]   K. E. Kurtis, P. J. Monteiro, Empirical models to predict concrete expansion

756   caused by sulfate attack, ACI Materials J. 97 (2000) 156-161 (errata publ. 97:713).

757   [9]   T. Ikumi, S.H.P. Cavalaro, I. Segura, A. Aguado, Alternative methodology to

758   consider damage and expansions in external sulfate attack modeling, Cem. Concr. Res.

759   63 (2014) 105–116.

760   [10]   C. Yu, K. Scrivener, Mechanism of expansion of mortars immersed in sodium

761   sulphate solution, Cem. Concr. Res. 43 (2013) 105–111.

762   [11]   R. Tixier, B. Mobasher, Modeling of Damage in Cement-Based Materials

763   Subjected to External Sulfate Attack. I: Formulation, J. Mater. Civ. Eng. 15 (2003) 305–

764   313.

765   [12]   R. Tixier, B. Mobasher, Modeling of damage in cementbased materials subjected

766   to external sulfate attack. II: Comparison with experiments, J. Mater. Civ. Eng. 15

767   (2003) 314–322.

768   [13]   B. Bary, Simplified coupled chemo-mechanical modeling of cement pastes

769   behavior subjected to combined leaching and external sulfate attack, Int. J. Numer.

770   Anal. Meth. Geomech. 32 (2008) 1791–1816.

771   [14]   S. Sarkar, S. Mahadevan, J.C.L. Meeussen, H. van der Sloot, D.S. Kosson,

772   Numerical simulation of cementitious materials degradation under external sulfate

773   attack, Cem. Concr. Compos. 32 (2010) 241–252.

774   [15]   A.E. Idiart, C.M. López, I. Carol, Chemo-mechanical analysis of concrete

775   cracking and degradation due to external sulfate attack: A meso-scale model,» Cem.

776   Concr. Compos. 33 (2011) 411–423.

777   [16]   X.B. Zuo, W. Sun, C. Yu, Numerical investigation on expansive volume strain in

778   concrete subjected to sulfate attack, Constr. Build. Mater. 36 (2012) 404–410.

779   [17]   N. Cefis, C. Comis, Damage modelling in concrete subject to sulfate attack,

780   Frattura ed Integrità Strutturale vol.:8 núm:29 (2014) 222–229.

781   [18]   B. Bary, N. Leterrier, E. Deville, P.L. Bescop, Coupled chemo-transport-

782   mechanical modelling and numerical simulation of external sulfate attack in mortar,

783   Cem. Concr. Comp. 49 (2014) 70–83.

784   [19]   Q. Nie, C. Zhou, H. Li, X. Shu, H. Gong, B. Huang, Numerical simulation of fly

785   ash concrete under sulfate attack, Constr. Build. Mater. 84 (2015) 261–268.

786   [20]   W. Müllauer, R.E. Beddoe, D. Heinz, Sulfate attack expansion mechanisms,

787   Cem. Concr. Res. 52 (2013) 208–215.

788   [21]   J.R. Clifton, J.M. Pommersheim, Sulfate attack of cementitious materials:

789   volumetric relations and expansions, NISTIR 5390, Building and Fire Research

790   Laboratory, Gaithersburg (MD), 1994.

791 [22]   G.W. Scherer, Stress from crystallization of salt, Cem. Concr. Res. 34 (2004)
792 1613–1624.
793 [23]   R.J. Flatt, G.W. Scherer, Thermodynamics of crystallization stresses in DEF,
794 Cem. Concr. Res. 38 (2008) 325–336.
795 [24] C.W. Correns, Growth and dissolution of crystals under linear pressure, Discuss
796 Faraday Soc 5 (1949) 267–271.
797 [25]   M. Steiger, Crystal growth in porous materials I: the crystallization pressure of
798 large crystals, J. Cryst. Growth. 282 (2005) 455–469.
799 [26]   W. Kunther, B. Lothenbach, K. Scrivener, Influence of bicarbonate ions on the
800 deterioration of mortar bars under sulfate attack, Cem. Concr. Res. 44 (2013) 77–86.
801 [27]   W. Kunther, B. Lothenbach, K. Scrivener, On the relevance of volume increase
802 for the length changes of mortar bars in sulfate solutions, Cem. Concr. Res. 46 (2013)
803 23–29.
804 [28]   M. Zhang, J. Chen, Y. lv, D. Wang, J. Ye, Study on the expansion of concrete
805 under attack of sulfate and sulfate-chloride ions, Const. & Build. Mat. 39 (2013),26-32.
806 [29] B. Gérard, J. Marchand, Influence of cracking on the diffusion properties of
807 cement-based materials. Part I: Influence of continuous cracks on the steady-state
808 regime, Cem. Concr. Res. 30 (2000) 37–43.
809 [30] D.A. Hordijk, Local Approach to Fatigue of Concrete, Phd Thesis, Delft
810 University of Technology, Delft, 1991.
811 [31]   I. Oliveira, S.H.P. Cavalaro, A. Aguado, New kinetic model to quantify the
812 internal sulfate attack in concrete, Cem. Concr. Res. 43 (2013) 95–104.
813 [32]   R. Tixier, Microstructural development and sulphate attack modeling in blended
814 cement-based materials, PhD Thesis, Arizona State University, Tempe, 2000.
815 [33]   P.W. Brown, An evaluation of the sulfate resistance of cements in a controlled
816 environment, Cem. Concr. Res. 11 (1981) 719–727.
817 [34]   A. Chabrelie, Mechanisms of Degradation of Concrete by External Sulfate Ions
818 under Laboratory and Field Conditions, PhD Thesis, ÉPFL, Lausanne, 2010.
819 [35] A. Kelly, Strong solids, Clarendon 1966.
820 [36] A. Jayatilaka, Fracture of engineering brittle materials, Applied Science
821 Publishers, 1979.
822 [37]   S. Oller, Simulación numérica del comportamiento mecánico de los materiales
823 compuestos, CIMNE 74 (2003).
824 [38] Y. Kaneko, H. Mihashi and S. Ishihara, Shear failure of plain concrete in strain
825 localized area, Proceeding of the Fifth International Conference on Fracture Mechanics
826 of Concrete and Concrete Structures, Colorado, USA, V.C. Li, C.K.Y. Leung, K.J.
827 Willam and S.L. Billington (ed.), 12-16 Vol.1 (2004) 383-390.
828 [39] B. Djazmati and J.A. Pincheira, Shear stiffness and strength of horizontal
829 construction joints, ACI Structural J. 101 (2004) 484-493.